

RESEARCH ARTICLE OPEN ACCESS

3D-Printed Dynamic Heart Model With Left-Side Anatomy and Integrated Sensor for Edge-to-Edge Repair and Regurgitation Reduction

Alejandro Guillen Obando¹ | Hongyi Shen¹ | Myles McGovern¹ | Yusen Zhang¹ | Vivien Lin¹ | Darryl Fu¹ | Ryan Baumwart²  | Kaiyan Qiu¹ 

¹School of Mechanical and Materials Engineering, Washington State University, Pullman, Washington, USA | ²College of Veterinary Medicine, Washington State University, Pullman, Washington, USA

Correspondence: Kaiyan Qiu (kaiyan.qiu@wsu.edu)

Received: 15 December 2025 | **Revised:** 26 January 2026 | **Accepted:** 20 February 2026

Keywords: 3D-printing | customized pressure sensors | dynamic heart model | edge-to-edge repair | embedded pneumatic actuation

ABSTRACT

Heart disease remains a major cause of morbidity and mortality in the United States, accounting for roughly 20% of all deaths. Minimally invasive procedures have been used to treat cardiovascular diseases; however, the heart's anatomical complexity and dynamics require proper hands-on training on patient-specific presurgical models to reduce procedural errors. Existing dynamic heart models often rely on animal cardiac tissues to support pumping mechanics, introducing ethical and policy concerns. Fully synthetic heart models offer an alternative by using actuation devices to reproduce cardiac circulation and contraction, yet accurately replicating the full dynamics of the heart remains challenging. This research presents a 3D-printed dynamic heart model representing left-side anatomy (atrium, ventricle, and mitral valve) to support minimally invasive procedures. Soft material 3D-printing is employed to replicate key anatomical features. Sutures anchor the ventricle to the mitral valve, replicating chordae tendineae-like structures, adding physiological realism and structural complexity. McKibben actuators are embedded within the myocardial walls, mimicking ventricular contraction and realistic mitral valve motion. Customized flexible pressure sensors are designed and incorporated to monitor pressure changes inside the model. These novel features enable the model to function as a platform for hemodynamic studies and simulation of edge-to-edge repair to mitigate atrioventricular valve regurgitation.

1 | Introduction

The cardiac system is a vital element of the human body's operation [1, 2] as the heart controls the pumping of blood throughout. Heart disease is the leading cause of death in the US [3, 4]; the American Heart Association (AHA) reported that over 82 million people are currently experiencing one or more types of cardiovascular diseases [3]. Over 800 000 Americans with severe heart diseases will undergo surgeries annually [5]. Similarly, morbidity caused by heart disease limits the ability of patients to perform routine tasks, including general self-care

and light physical activities, degrading their quality of life [6]. Rigorous training and observation have been the traditional ways for a cardiac surgeon to become competent. Therefore, models and simulations can help enhance procedural success, minimize medical errors, and reduce cognitive load [7]. Incorporating both dynamic and anatomically accurate elements [8] allows a more realistic model for an individualized rehearsal for cardiac surgeries and interventions. Rehearsals with models are currently performed in minimally invasive procedures on a beating heart, such as mitral [9] or aortic [10] valve repair and device implantation, where realistic motion and spatial fidelity are

This is an open access article under the terms of the [Creative Commons Attribution](https://creativecommons.org/licenses/by/4.0/) License, which permits use, distribution and reproduction in any medium, provided the original work is properly cited.

© 2026 The Author(s). *Advanced Materials Technologies* published by Wiley-VCH GmbH

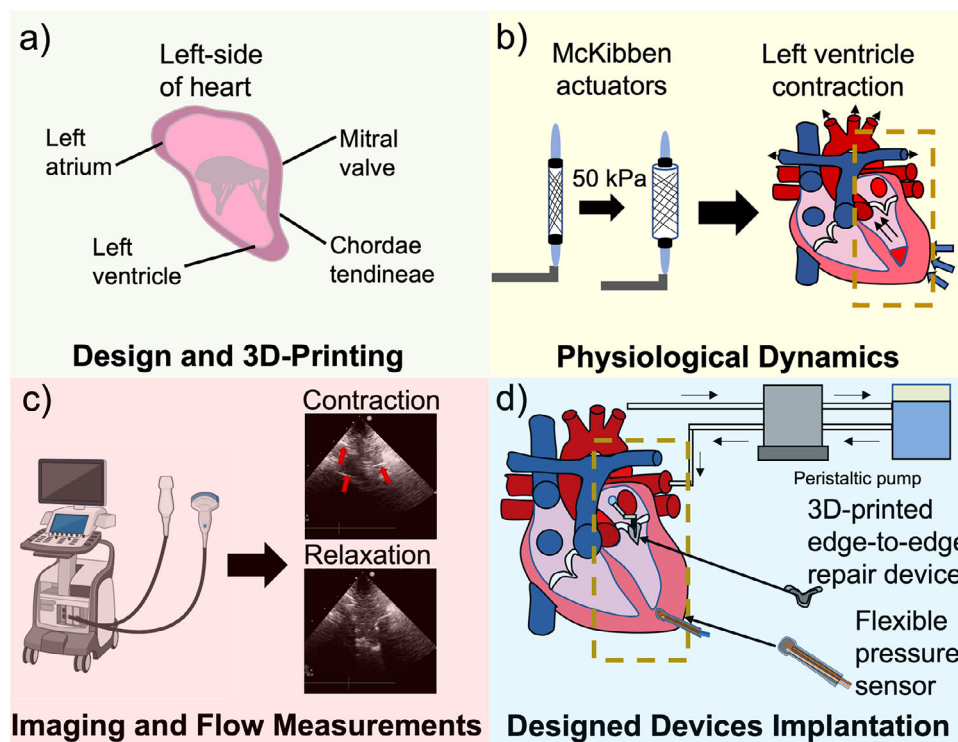


FIGURE 1 | Design of a 3D-printed heart model with left-side anatomy and the incorporation of EERD in the model for surgical practice, along with a fully circulatory system. (a) Design and 3D-printing of the heart model with left-side anatomy and all developed components. (b) Incorporation of embedded McKibben actuators for left ventricle contraction. (c) Ultrasound imaging is used to observe mitral valve performance, with observed flow and regurgitation measurements. (d) Implantation of a 3D-printed EERD in the mitral valve and customized pressure sensors in the left ventricle with an incorporated mock circulatory loop for surgical practice.

critical. Current model rehearsals, however, are not commonly patient-specific models.

To prepare surgeons for medical interventions in the heart, different presurgical models have been developed [11–13]. These models vary from computer-based, focusing on augmented or virtual reality [14], or physical models (animal and cadaver hearts [15], bioprinted heart models [16–19], and synthetic heart models). All these approaches provide advantages, such as visualization of intricate features in computer-based models and soft, tissue-like features in physical models. However, they all present limitations. Due to being strictly visual, computer-based models prevent kinesthetic learning [20]. In physical models, the use of animal and cadaver hearts lacks patient-specificity and reusability [15] while also raising potential ethical [21] and policy [22] issues. Regarding bioprinted heart models, two major techniques have emerged for cardiac cell growth in heart models: freeform embedding of suspended hydrogels (FRESH) for high fidelity [16, 19] and sacrificial writing into functional tissue (SWIFT) for creation of vesicles in a high cell density tissue [17]. These methods introduce cardiomyocytes into the model/scaffold that can contract spontaneously. Although promising, engineered cardiac tissue produces much lower strain (2%) than the human myocardium (30%) [23] and thus cannot exert enough pressure to pump blood continuously. In addition, bioprinted heart models suffer from multiple other issues [24–26], such as insufficient vascularization, immature and scarce cardiomyocyte sources, poor electrical and mechanical integration with host tissue, and challenges in cell viability and scalability.

The use of synthetic heart models can help overcome limitations of computational and bioprinted systems by more accurately replicating cardiac dynamics and anatomy [27]. The heart contains complex physiological features, causing some of these synthetic models to lean into either anatomical accuracy [28] or dynamics [29], but not both. The heart's contraction dynamics are controlled by myocardial muscles; these contain different muscle fiber orientations (circumferential, radial, and longitudinal), making it difficult to accurately replicate their structure and behavior simultaneously [30]. Through pneumatic actuation [31, 32], the synthetic models have been able to mimic myocardium dynamics. However, these models have relied on the assistance of animal organs to reproduce hemodynamics in a mock circulatory loop [32–34]. Hydraulic actuation has emerged as a promising alternative, where fibers are incorporated in the model to enable contraction through hydraulic pressure [30]. The fiber orientation obtained in the developed cardiac sleeves allows for accurate contraction dynamics without the need of animal hearts [35]. However, in these models, the helical design causes the actuators to elongate axially rather than contract, whereas pneumatic actuators contract axially and expand radially [36], with the latter having more physiologic contraction dynamics. Additionally, the complex physiology of the heart has led to simplified dynamics, focusing on certain chambers of the heart (especially the left ventricle) [37–40], leading to a lack of exploration of the interactions between the heart's components.

Even as current synthetic models present a promising approach to replicate heart dynamics, they lack anatomical accuracy, creating

a tradeoff between fidelity and accurate dynamics. In the previously reported synthetic heart models, 3D-printed molds were used to cast soft polymer-based materials to reproduce ventricular structures [30–32]. Then, a robotic sleeve was wrapped around the molded structure to achieve contraction, through pneumatic or hydraulic actuation [31, 35]. While this approach permits contraction in the model, many of the heart's intricate features, such as the curvature found in chambers, and the presence of elements such as papillary muscle or chordae tendineae, are not replicated. 3D-printing has been previously used to manufacture anatomically accurate heart models for visualization due to its layer-by-layer approach, enabling the development of intricate features. Printing methods such as fused deposition modeling (FDM), stereolithography (SLA), and digital light processing (DLP) have been used for the fabrication of these models [41–44]. While promising, these methods generally only develop rigid structures; to replicate the heart muscle's dynamics, softer materials that assimilate the myocardium's mechanical properties are necessary. Through direct ink writing (DIW), polymer-based inks (silicone-based) used to 3D-print organ models have been demonstrated [45, 46], even expanding into the 3D-printing of an aortic root [10]. Silicone-based inks are widely used due to their transparency, biocompatibility, elastomeric properties, and chemical and thermal stability [47]. Even so, the simultaneous replication of anatomical accuracy and dynamics remains difficult due to the complexity of the myocardial architecture, compromising the ability to provide physiological contraction. The ability to fabricate precise sections through 3D-printing can be beneficial to develop a more anatomically accurate heart model while retaining the softness required to generate contraction [44–46].

The left ventricle generates the highest pressure in the heart [48, 49]. Therefore, several disease etiologies can alter the left ventricle's functionality [50]. The left ventricle's blood flow from the left atrium is controlled by the opening and closing of the mitral valve. During diastole, ventricular relaxation and atrial contraction both allow mitral valve opening and left ventricle filling. During ventricular systole, pressure generated in ventricular contraction maintains a closed mitral valve, and blood is ejected through the aorta. Mitral valve regurgitation commonly occurs due to altered coaptation pressure gradient between the left atrium and left ventricle [51]. This can lead to enlargement of the left atrium and eventual heart failure [52–54]. Mitral regurgitation can be mitigated by currently developed edge-to-edge repairs using minimally invasive surgical methods, allowing alternatives to open-heart surgery.

To address these concerns, this work demonstrates the development of a novel soft, dynamic 3D-printed heart model focusing on the left-side anatomy (ventricle, atrium, and mitral valve) (Figure 1a) with embedded McKibben actuators, enabling contraction dynamics in the model (Figure 1b). Imaging techniques (ultrasound and endoscope) are used to visualize the hemodynamic behavior of the model (Figure 1c), and its performance is tracked before and after the insertion of a 3D-printed edge-to-edge repair device (EERD) with the assistance of customized flexible pressure sensors in a mock circulatory loop (Figure 1d). The novelty and rationale of our work include: (i) The use of 3D-printing for the development of a soft dynamic heart model, departing from traditional mold-casting methods that require multiple fabrication stages [30–32], as well as from

conventional 3D-printed models that lack dynamic functionality. (ii) The incorporation of unique anatomical features in the heart model in the form of the inclusion of chordae tendineae in the mitral valve and left ventricle through suturing (the mitral valve was sutured on top of the left ventricle). These sutures were then placed through the ventricle, acting as the chordae tendineae. This novel component regulates valve opening and closure through its contraction mechanism [55] and replicates more realistic surgical conditions. (iii) Integration of McKibben pneumatic actuators directly within the myocardial wall [56], to reproduce physiologically realistic left-ventricular contraction capable of driving naturalistic mitral valve opening and closure. The integration of these actuators in the 3D-printed cardiac walls contrasts with prior models [30–32, 37, 57] relying on cardiac sleeves, creating a less intrusive approach for contraction, and facilitating surgical practice. (iv) The fabrication of customized flexible piezoresistive sensors for strategic incorporation and accurate pressure measurements in the heart model. Together, this strategy yields a dynamic heart model with physiologically accurate structures capable of generating realistic hemodynamic conditions for practicing surgical device implantation aimed at mitigating mitral valve regurgitation. It reduces reliance on animal organs and offers a more anatomically faithful internal architecture than what is typically achievable with casted models [58–60], granting the ability to fabricate patient-specific heart models for surgical simulation.

2 | Results and Discussion

2.1 | Development of Silicone-Based Ink

To develop printing inks with mechanical properties of cardiac tissue, silicone sealant (active agent) and silicone grease (bulking agent) were initially mixed at different ratios to find approximate values close to the myocardium's Young's modulus. Silicone-based materials were selected due to their relatively high 3D-printing resolution, as well as their curing process elevating their mechanical properties at a range approaching the one found in heart tissue (as low as 8–10 kPa in diastolic phase [61], with silicone inks as low as 10–20 kPa [45]). The vulcanization process at room temperature of the active agent helps stabilize the printed structures. Incorporation of the bulking agent inhibits the curing rate, ensuring adequate printability while increasing softness in the material [62]. However, in large prints, the excess of bulking agent can cause the layers in the print to collapse. Modification of the component ratios enables controlled tuning of the mixture's mechanical properties to approximate those in the myocardium. The average Young's modulus values for inks formulated with different weight ratios of active and bulking agents are presented in Figure 2a. As the proportion of bulking agent increases (from 0 to 2:1 w/w bulking to active agent ratio), the Young's modulus correspondingly decreases. Specifically, with no presence of bulking agent, the Young's modulus was 698 kPa, while observing a noticeable drop at the highest bulking to active agent ratio (2:1, w/w), with a Young's modulus of 52 kPa. A report demonstrated that a fibrotic myocardium presented a Young's modulus of 55 kPa, and myocardial tissue over 100 kPa in the systolic phase [63]. An approximate value was observed in the 1:1 (w/w) ratio mixture of our printing ink (123 kPa). The 1:1 (w/w) ratio ink was selected in this work due to the printability

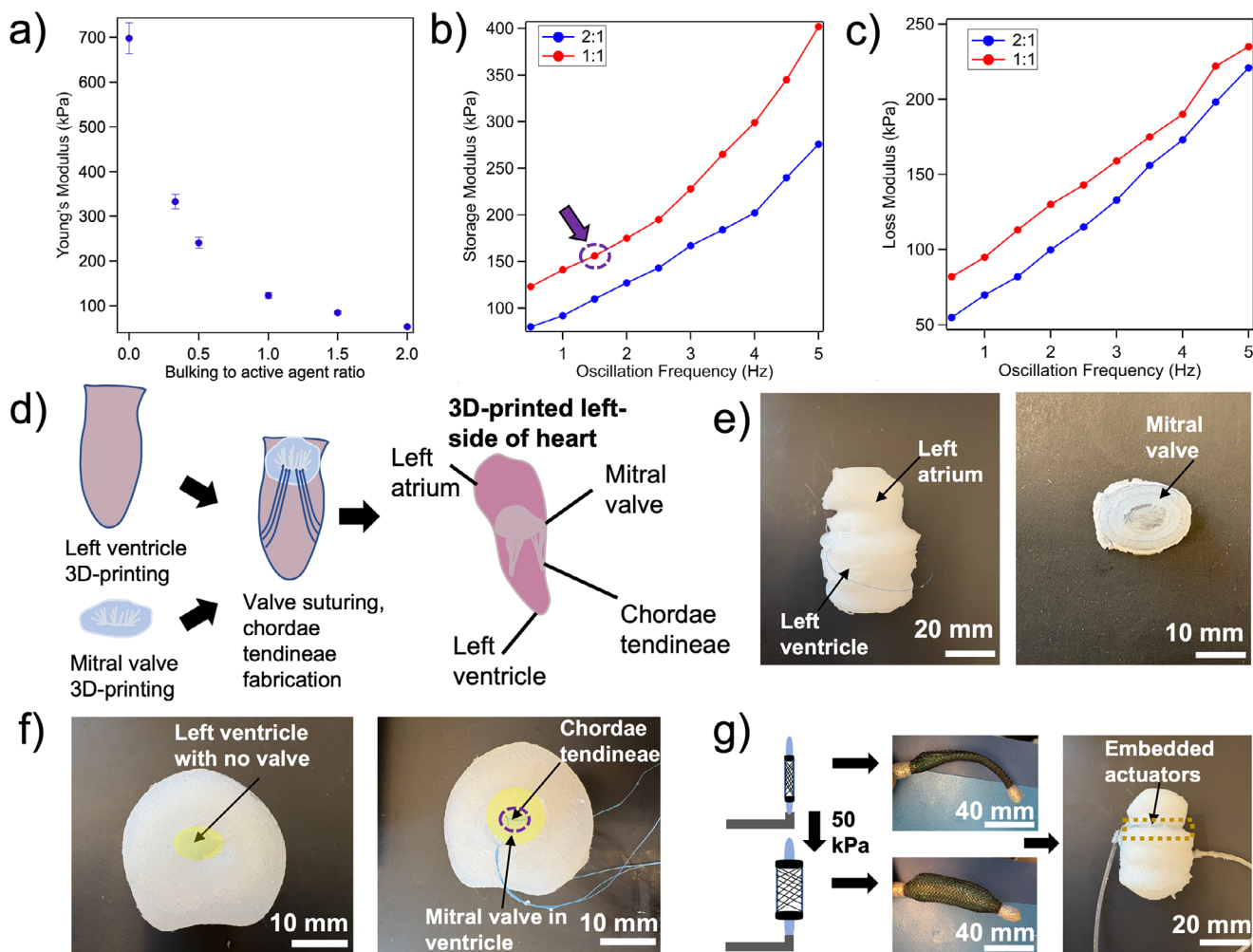


FIGURE 2 | Design and fabrication of a 3D-printed heart model with left-side anatomy. (a) Young's modulus of printing inks with respect to different ratios (w/w) of the bulking to active agent. (b) Storage modulus of printing inks with distinct ratios of bulking to active agent with respect to oscillation frequency. (c) Loss modulus of printing inks with distinct ratios of bulking to active agent with respect to oscillation frequency. (d) Design and 3D-printing of a left atrium and ventricle with an incorporated mitral valve. (e) Images of the 3D-printed model (left) and the mitral valve (right), respectively. (f) 3D-printed left ventricle before mitral valve incorporation (left) and incorporation of mitral valve in 3D-printed left ventricle, using sutures that act as chordae tendineae (right). (g) Design and functionality of embedded McKibben actuators, displaying a schematic (left) and images (middle) of the actuators before and after being pressurized, and their embedding in the left-side heart model (right).

advantage given by it. Other mixtures with a higher bulking-agent ratio (such as a 2:1 w/w ratio) were evaluated; however, the increased proportion of bulking agent slows crosslinking, and the supporting material (Pluronic F127) trapped within the complex structure printed further prolongs curing time, ultimately causing the model's layers to collapse.

Different mixtures of the active and bulking agents were mechanically tested to determine their Young's modulus, allowing identification of a formulation that approximates heart tissue while retaining good printability. Once a good mixture candidate (1:1 w/w ratio) was determined, its storage and loss moduli were used to study the mixture's viscoelastic behavior at different oscillation frequencies. The 2:1 (w/w) ratio mixture was also characterized to confirm viscoelastic behavior across inks with comparable moduli to those observed in the myocardium. To understand the dynamic properties of these materials, dynamic mechanical analysis (DMA) was performed. Here, the materials

were oscillated at a frequency range from 0.5 to 5 Hz. This frequency range was previously observed in human tissue measurements [64], and the oscillation frequency test was chosen to prove the silicone-based ink's viscoelastic behavior, like that of myocardium (cardiac tissue) [65]. An increase in both storage and loss moduli was observed (Figure 2b,c) as the oscillation frequency increased. This is a common behavior on both moduli for viscoelastic materials, proving their tissue-like properties [66]. At 1.5 Hz, approximating the frequency of the beating heart [67], the 1:1 (w/w) ratio formulation shows a storage modulus of 110 kPa and a loss modulus of 82 kPa (Figure 2b), values that align with the myocardium's systolic-phase Young's modulus. Interestingly, the difference in loss modulus (Figure 2c) between the printed ink with a larger amount of bulking agent (2:1 w/w ratio) increased at a faster rate than that with less (1:1 w/w ratio). This is due to the dispersion of forces caused by the softer material, allowing for polymer chains to move more freely.

2.2 | Design and Fabrication of the Heart Model With Left-Side Anatomy

A fabrication process to develop a 3D-printed heart model with left-side anatomy was put in place, as shown in Figure 2d. First, the left ventricle was 3D-printed using the 1:1 (w/w) ratio mixture of active and bulking agents selected, using DIW as a printing technique. The mitral valve was printed separately with induced defects in the posterior leaflet, then sutured in the annulus, with additional sutures used to mimic chordae tendineae. Both the 3D-printed model and the mitral valve were imported from computer-aided design (CAD) by Solidworks and later sliced in Slic3r software to fit the parameters of the DIW printer being used. Images of the standard tessellation language (STL) files for both the fully designed 3D-printed heart model with left-side anatomy and its respective mitral valve are shown in Figure S1. After the mitral valve was inserted into the left ventricle, the ventricle was repositioned precisely on the printing bed, and the left atrium was subsequently printed, completing the 3D-printing process (Figure 2e left). In the 3D-printing process, supporting material ink was used to hold the printed ventricle in position. The ventricle is largely hollow with an incorporation of a half-inch-diameter outlet, which improves flow through the system. The model's myocardium presents curvature in different regions of the model. This was designed to assimilate the heart's curved features utilizing 3D-printing's layer-by-layer approach to create more complex structures. Wall thickness in the heart model varies from 2.1 to 30.4 mm. After the printing of the left ventricle was completed, the mitral valve was printed separately (Figure 2e right). The valve was designed to fit the diameter of the left ventricle's chamber on its top section (Figure 2f left). The posterior leaflet of the mitral valve was purposely designed to be of a larger size than the anterior leaflet, generating defective closure of the mitral valve when contracted. The posterior leaflet was set at 6.18 mm in width, while the anterior leaflet was set at 4.88 mm. The mitral valve's thickness (from top to bottom) was set at 7.65 mm to stabilize and properly place the mitral valve in the annulus. Prior to inserting the mitral valve into the chamber, sutures were placed on each of the leaflets of the 3D-printed valve. Here, a needle was used to insert the sutures in both the anterior and posterior leaflet of the mitral valve. The sutures were then threaded through the left ventricle, with multiple passes made to generate tension between the sutures and the ventricular walls. This configuration effectively created a structure mimicking the chordae tendineae within the model (Figure 2f right; Figure S2). It has been reported that one of the major challenges in minimally invasive surgical practice is the interference caused by the chordae tendineae emerging from the mitral valve [68]. The incorporation of this structure provides a more accurate representation of the left ventricle's anatomy, which is difficult to reproduce through 3D-printing due to the thin geometry of the tendons and the constraints of layer-by-layer fabrication. The addition of sutures did not present any delamination effects on the mitral valve, as the tension generated by these is not enough to cause delamination on the valve.

After these components were incorporated, the model was repositioned at the same coordinates (marked on the printing bed) to resume the printing process. The atrial section was then printed [68]. Through this method, our 3D-printed heart model with left-side anatomy was fabricated, with the inclusion of a ventricle, an

atrium, and a mitral valve, as well as the added sutures that can act as chordae tendineae (Figure 2e,f).

In addition to the model fabrication, actuators were incorporated into the system to aid in the contraction of the mitral valve. Inspired by previous work [31, 32], McKibben actuators (Figure 2g left and middle) were used to replicate myocardial contraction in the left ventricle. Upon pneumatic pressurization, the actuators contracted axially and expanded radially inside the ventricular walls, effectively closing the mitral valve and reproducing the systolic phase of the cardiac cycle. The manufactured McKibben actuators (Figure 2g left) and their radial expansion when exposed to pneumatic pressure (50 kPa) are shown in Figure 2g (middle). Images displaying the construction of the McKibben actuators are presented (Figure S3), and their step-by-step fabrication is discussed in the experimental section of this work. Following fabrication, the actuators were integrated into the walls of the 3D-printed left ventricle (Figure 2g right) to generate ventricular contraction and regulate mitral valve opening and closure within the model. The design flexibility of 3D-printing enabled the incorporation of precisely dimensioned entryways within the walls of the left-ventricle to accommodate the actuators, each sized to fit a quarter-inch diameter. The sliced STL file reveals the circumferential direction of the two channels used to embed the actuators into the ventricular walls (Figure S1d,e). The orientation of the channels around the left ventricle causes circumferential shortening as the actuators contract. The actuators controlled the induced heart rate in the model and operated at 70 beats per minute (bpm), which approaches that of the human heart (72 bpm). The myocardium contracts in three different directions, circumferential, radial, and longitudinal [69], and achieving this through pneumatic actuation has proven difficult [56]. This work demonstrates circumferential and radial shortening, yet not longitudinal (Movie S1). In pneumatic actuation of synthetic heart models, these contraction dynamics have been previously demonstrated, but only through simplified geometries or by integrating external cardiac sleeves to house the actuators.

2.3 | Imaging of 3D-Printed Mitral Valve in the Dynamic Heart Model

To ensure proper performance of the 3D-printed heart model and mitral valve, endoscopic and ultrasound imaging techniques were performed to observe the mitral valve's functionality under contraction. This was achieved by integrating the heart model with left-side anatomy into a circulation loop system, using the 3D-printed inlet at the atrium and outlet at the ventricle to drive a blood-mimicking glycerol-water fluid through the system. The fluid was pushed through using a peristaltic pump (Golander BT 101S Variable-Speed Peristaltic Pump) to assimilate the cardiac circulation dynamics. The geometry of the heart model and the dynamics of mitral valve contraction governed the resulting flow rates. First, we observed mitral valve opening and closure driven solely by its contraction dynamics (in the absence of flow) in Figure 3a,b. The opening and closure of the mitral valve were also observed in Movie S2. The images were taken without flow, as the fluid makes the endoscopic imaging more challenging. Here, we observed a mitral valve that can close as it is compressed by the McKibben actuators embedded in the model. As discussed, in the systolic phase of the heartbeat, the left ventricle contracts

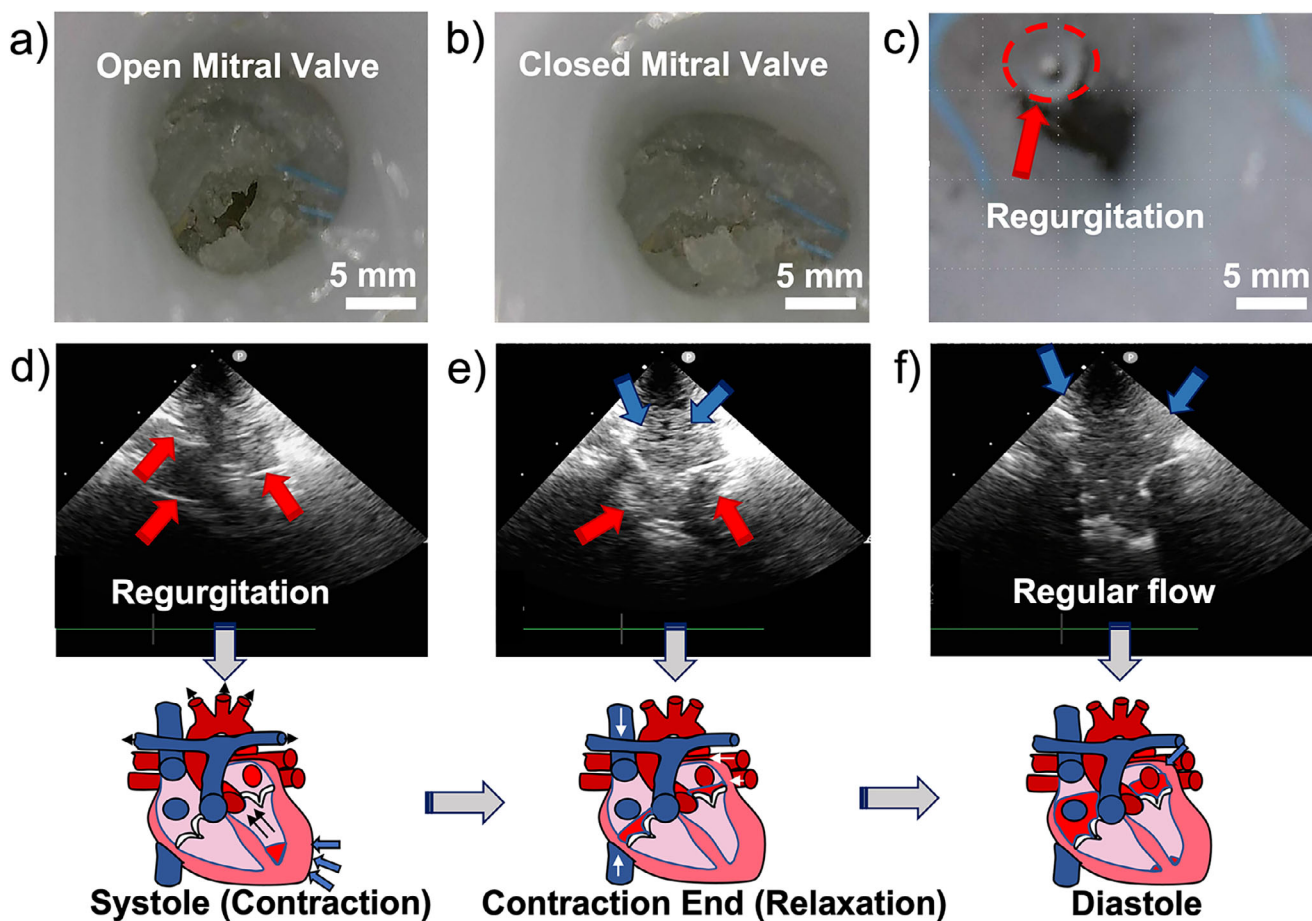


FIGURE 3 | Endoscopic and ultrasound imaging of the mitral valve. (a) Opening and (b) closure of the mitral valve through endoscopic images. (c) Mitral valve with flow, observed after contraction. (d–f) Ultrasound images of the mitral valve (with a blue, downward arrow indicating regular flow and a red, upward arrow indicating regurgitation), (d) before, (e) during, and (f) after ventricular contraction, offered by the presence of McKibben actuators, with the respective cardiac cycle phases replicated in a corresponding schematic.

and the mitral valve closes, indicating our model accurately mimicked the cardiac dynamics. This was controlled by the applied pressure of the actuators. To further understand the influence of the actuators in contraction dynamics, contraction strain was measured by taking still images during diastole and systole of the upper region of the left ventricle (Figure S4). In the upper region of the ventricle, the wall thickness measured at 23.4 mm. The ventricular walls exhibited a displacement of approximately 4.1 mm from their relaxed state, giving a contraction strain of 17.5%. As the actuators were constrained by being embedded in the ventricular walls, they were unable to operate at full capacity. Typically, these actuators can contract between 25% and 35%, consistent with what was observed in literature [70]. An image of an open mitral valve with flow was observed in Figure 3c. In this image, the red arrow indicates a bubble generated by regurgitant flow during mitral valve closure. Regurgitation results from the induced defects in the mitral valve and the use of a deliberately non-pulsatile pumping system. Together, these reproduce the hemodynamics observed in mitral valve disease, characterized by incomplete contraction and reduced flow [71].

To further assess the flow dynamics within the model, ultrasound imaging was employed to visualize both the motion of the mitral valve and the movement of the blood-mimicking fluid.

Ultrasound imaging through silicone-based materials can prove difficult, as the presence of entrapped air bubbles in the cured ink can act as “mirrors” in the system [72]. To mitigate this issue, thinner walls (~2 mm) were printed in areas of the atrium, and a cutout was designed in the atrial chamber to allow the ultrasound probe to enter the model and contact the fluid directly, helping obtain clearer ultrasound imaging of the mitral valve [73]. To obtain clear images, heart models are generally submerged in a water bath for optimized ultrasound measurements. However, because mitral valve contraction is driven by the McKibben actuators, the 3D-printed model could not be submerged, which made ultrasound imaging more difficult. Due to the difficulty of obtaining ultrasound images in the 3D-printed model, Doppler imaging was not obtained from ultrasound imaging, a limitation in our study. Generally, Doppler imaging is measured through sound waves and their interactions with red blood cells, which are not included in our blood-mimicking fluid [74]. The effects of the flow rate in the 3D-printed model were more pronounced in Figure 3d–f, where ultrasound was used to observe regions of regurgitation (red arrows) and regular flow (blue arrows) in the atrial section of the model. This was done in the model during systole contraction (Figure 3d), right after contraction (Figure 3e), and in the diastole relaxation phase (Figure 3f) of contraction in the left ventricle of the model. As it can be seen in Figure 3d, as the

valve contracted, flow partially started to regurgitate back into the atrium. Due to the synthetic nature of the valve, it is not expected to fully behave as a native valve, unless external assistance is provided, such as animal organs or intricately designed pumps. As the valve relaxed, forward flow began to re-establish with only minor residual regurgitation (Figure 3e), and normal flow fully resumed once the ventricular chamber returned to its relaxed state (Figure 3f). A full loop of this process can be observed in Movie S3. These observations indicate that regurgitation in the mitral valve is produced due to the induced defects in the mitral valve and the generation of non-pulsatile inflow entering the model. Such conditions are induced to replicate mitral valve disease conditions. Even so, the valve was still able to function normally, responding appropriately to left-ventricular contraction and maintaining its expected opening-closure behavior.

2.4 | Replication of Defective Mitral Valve and Integration of 3D-Printed EERD for Partial Regurgitation Reduction

The effects of regurgitation in the model, applied pressure from the actuators, and the regurgitation of blood-mimicking fluid were studied. First, the applied pressure required from the actuators to achieve mitral valve closure was recorded. Ultrasound imaging was then used to understand the effect of the applied pressure in the model by observing its regurgitation patterns through contraction in the ventricle. The increase in actuator pressure caused more regurgitation, thus decreasing the flow rate and pressure in the model. In Figure S5, endoscopic images revealed that the mitral valve only achieved full closure through contraction when the actuators applied 200 kPa of pressure. Pressures below this level (25, 100, and 180 kPa) were insufficient to induce valve closure. The effects on the regurgitation patterns on the heart model were then tracked in Figure 4a. Here, ultrasound imaging was employed to monitor atrial flow as the model completed two relaxation-contraction cycles. Normal flow was observed before the first contraction (Figure 4a₁), and regurgitation with higher intensity was observed as it contracted (Figure 4a₂). As the model entered its second relaxation phase (Figure 4a₃), the flow remained unstable, and during the subsequent contraction, the regurgitation became more pronounced (Figure 4a₄). A full cycle of this process through ultrasound imaging is shown in Movie S4. To prevent major regurgitation, a 3D-printed EERD was then fabricated using SLA. The EERD was designed to simulate commercial MitraClip medical devices [75]. Its presence aids in the reduction of regurgitation of blood in the heart, stabilizing its movement and its pressure. The EERD was inserted in the mitral valve of the model, as shown in Figure 4b. Typically, minimally invasive edge-to-edge repair is delivered via a catheter through the left atrium and positioned at the mitral valve to achieve a proper fit [76]. Here, we implanted the 3D-printed EERD by guiding it through the inlet into the model and positioning it on the mitral valve, applying a small amount of silicone sealant to secure it in place. This modification enabled full valve closure at lower applied pressures (Figure S6). The substantial regurgitation observed during mitral valve closure also influenced the flow rate within the 3D-printed heart model. The correlation between flow rate and applied pressure is shown in Figure 4c. At an applied pressure of 200 kPa, the flow rate (437 mL/min) decreased by

15% relative to the baseline value (511 mL/min) measured when the model was not contracting. The incorporation of this EERD lowered the pressure required to fully contract the valve from 200 to 110 kPa (Figure 4c), reducing regurgitation seen at the higher applied pressures. The flow rate at this pressure increased to 479 from 437 mL/min, a 10% increase (Figure 4c). As in flow rate, the ejection fraction and stroke volume increased as the EERD was inserted in the mitral valve. Here, we observed a change in stroke volume from 6.43 to 7.04 mL, corresponding to an ejection fraction increase from 48% to 53%. All comparative values of the 3D-printed model's hemodynamic performance before and after the insertion of the EERD are displayed in Table S1. The reported ejection fraction was consistent with values from other synthetic heart models and, after incorporation of the EERD, fell within the normal range observed in healthy human hearts (50%–70%) [56, 77]. It is anticipated that the initial reduced flow rate also influenced the model's ventricular pressure; as the ventricle contracts more forcefully, it stiffens, leading to a corresponding drop in intraventricular pressure [78, 79]. With the aid of a piezoresistive pressure sensor designed and fabricated in our lab (Figure 4b), the pressures in the left ventricle were recorded. The sensor's flexibility and water resistance allow it to be placed in any region of the model without experiencing electrode interference and provide superior measurement adaptability compared to commercial sensors. The sensors are inserted through the heart model's outlet in the left ventricle, and then strategically placed in the top section of the chamber for proximity to the contracting areas in the model. Since synthetic models cannot faithfully reproduce physiological behaviors like arterial strain during contraction, the use of integrated sensors becomes essential for accurate measurement. The piezoresistive sensor is able to record pressures in the systolic and diastolic phases of contraction in the left ventricle. As the mitral valve opens and closes, it generates pulsatile flow within the left ventricle and produces a corresponding pressure change with each contraction. Pressures observed at the systolic phase of the model, recorded before and after the incorporation of the EERD, are shown in Figure 4d. After edge-to-edge repair, we observed an increase in the systolic pressure from 45.2 to 67.4 mmHg, an expected behavior following the reduction in mitral valve regurgitation. Normally, the left ventricular systolic pressure of a healthy human heart can vary between 100 and 120 mmHg. Because this model is fully synthetic and does not rely on animal cadaver hearts or complex pump-based systems, and because it lacks key physiological features such as arterial and venous strain during ventricular contraction, it is not currently able to generate the high pressures reported in other studies [56, 77, 80]. Even so, the incorporation of the EERD reduces mitral valve regurgitation during contraction (Figure 4e). Here, the ultrasound images demonstrate that the mitral valve can progress through its contraction and relaxation phases of the cardiac cycle without exhibiting major regurgitative flow (Movie S5). This reduction in regurgitation is likely due to the decreased pressure required to achieve valve closure when the 3D-printed EERD is in place. At these lower applied pressures (after edge-to-edge repair), the pneumatic actuators cause the 3D-printed ventricular walls to contract less forcibly, limiting the frequency of regurgitation observed in the model. Through hemodynamic testing, the 3D-printed model presented slight leakage and no notable delamination. With the development of more complex iterations of these 3D-printed heart models, understanding the effects of fatigue will be valuable. With the simulated integration

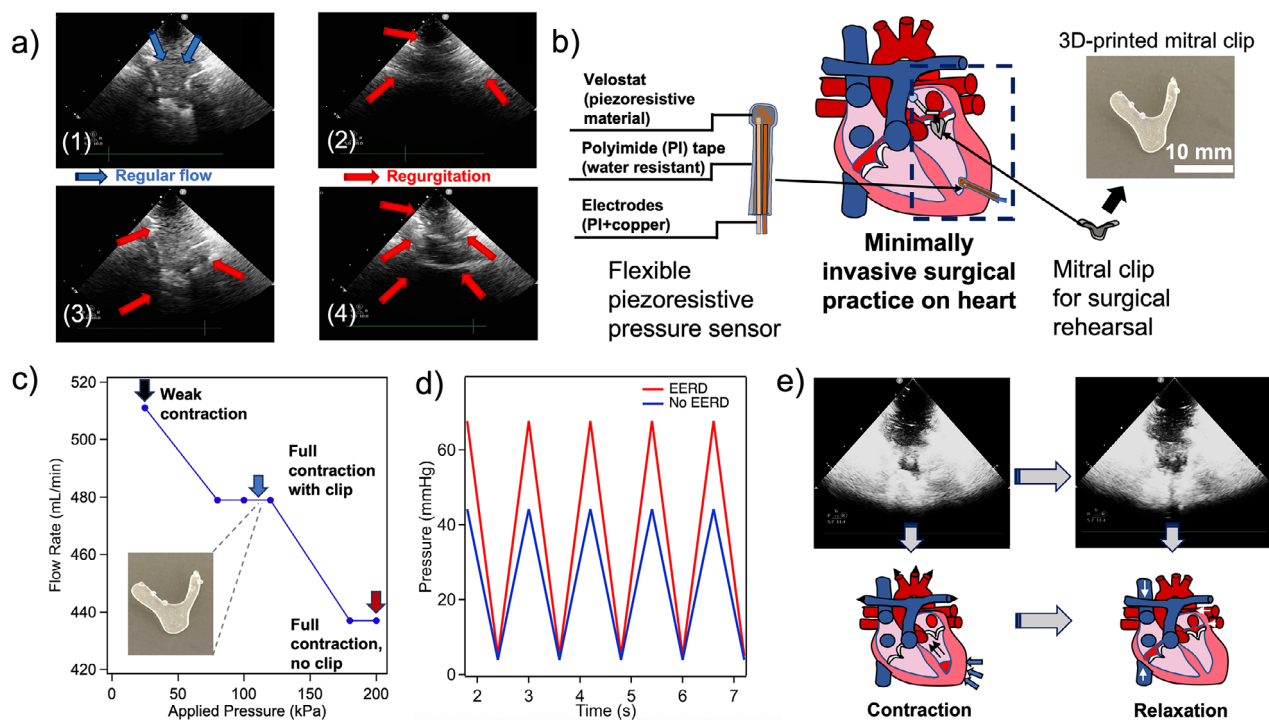


FIGURE 4 | Mitral valve regurgitation and edge-to-edge repair using a 3D-printed EERD. (a) Ultrasound imaging of the mitral valve during two cycles of contraction, split into four images: (a₁) before the first contraction, (a₂) during the first contraction, (a₃) before the second contraction, and (a₄) during the second contraction. (b) Schematic demonstrating the implantation of the 3D-printed EERD into the heart model to reduce regurgitation and integration of the designed piezoresistive pressure sensor. (c) Flow rate recorded in the left-side heart model with respect to applied pressure in three major stages: weak valve contraction (constant flow, no regurgitation), full contraction with the assistance of a 3D-printed EERD, and full contraction without the assistance of an EERD. (d) Pressure waveforms recorded in the left ventricle before and after insertion of the EERD with respect to time. (e) Ultrasound imaging of the mitral valve during the contraction and relaxation phases of the cardiac cycle with an incorporated EERD, significantly reducing regurgitation.

of the EERD, the 3D-printed heart model developed in this work demonstrates its utility as a surgical training and rehearsal platform, enabling surgeons to practice the EERD implantation and compare outcomes between a regurgitant mitral valve and one that is properly corrected. In addition, suturing the mitral valve into the model enables its reuse across different patient-specific heart models and allows for closer examination of the valve both with and without the EERD.

3 | Conclusions

This work presents the development of a 3D-printed model of the left side of the heart, with both anatomical and physiologically simulated features. This model is produced using a two-step printing process that allows integration of a 3D-printed mitral valve with built-in sutures functioning as chordae tendineae, an element that has been difficult to replicate in previous surgical models. In the heart model design, dedicated channels were incorporated into the ventricular walls to house McKibben actuators, enabling controlled chamber contraction and resulting in functional mitral valve motion. In terms of hemodynamic performance, regurgitation patterns were observed due to induced defects in the mitral valve, and these were mitigated following use of the 3D-printed EERD. Flexible, water-resistant pressure sensors are also incorporated in the model's left ventricle, offering accurate readings in the systolic and diastolic phases

of contraction. The 3D-printed design allows for the simulation of clinically relevant surgical procedures without the need for animal organs. Building on this foundation, the future stage of this work aims to extend these capabilities toward a full heart model by creating an anatomically and physiologically accurate representation of the human heart. By examining valve-chamber interactions in this work, we establish a platform that can be expanded to more advanced designs in the future, including a fully dynamic four-chamber heart model. Fully soft heart models with four dynamic chambers have yet to be realized, highlighting the need for systems that can pair anatomical fidelity with physiological dynamics. Such models, while currently valuable for surgical training, also provide a foundation for developing total artificial hearts by leveraging the soft materials and fine structural resolution enabled by additive manufacturing.

4 | Experimental Section

4.1 | Customized Polymeric and Supporting Ink Formulation for 3D-Printing

The printing ink compound was formulated with a bulking agent: silicone grease (#LP20, Trident) and an active agent: silicone sealant (Loctite SI 595 CL with acetoxycuring and room temperature vulcanization). The weight ratio of the bulking agent to active agent for the ink was 1:1 (w/w). These substances were

mixed via a centrifugal mixer (ARE-310, Thinky) at 2000 rpm for 2 min. The supporting ink consisted of Pluronic 127 (Sigma-Aldrich) dispersed in a glycerol/deionized water solution (1:9 v/v) with a 2:5 (w/v) ratio and provided temporary structural assistance for overhanging and complex model features.

4.2 | Mechanical Properties of the Customized Ink

Following ASTM guidelines, we fabricated a series of cylinders (10 mm diameter, 15 mm height) using various bulking-to-active-agent ratios (0:1, 0.33:1, 0.5:1, 1:1, 1.5:1, and 2:1 w/w). To evaluate their mechanical properties, we subjected these cylinders to a static compression test using specialized mechanical testing equipment (Instron 600DX). During the test, a load cell with a capacity of 50 lbs was utilized and traveled a distance of 9.5 mm downward at a controlled rate of 0.5 mm/s. Data collection was performed on the initial stress deformation behavior at the strain range between 0.00 and 0.30, which corresponds to a stress range of 0–100 kPa. To gather dynamic mechanical behavior information, these cylinders were subject to an oscillation frequency test. Here, the cylinders were compressed 5 mm at varying oscillation rates, ranging from 0.5 to 5 Hz, following the ranges of the human body's muscle frequency, and that of the heartbeat (1.5 Hz). Storage and loss moduli of different inks were then recorded and used to determine the optimal customized ink to be used in the development of the 3D-printed heart model.

4.3 | 3D-Printing of the Heart Model

The human heart's STL model was designed based on the organ's anatomy and simplified to have space for the incorporation of the mitral valve and McKibben actuators. Here, curvature was minimized in the regions close to the mitral valve to provide sturdiness as it was sutured. Thickness in the walls was significantly increased to 28 from 2 mm in the regions where the McKibben actuators were incorporated. The heart model's volume was the following: 75.65 (L) × 70.42 (W) × 105.23 (H) mm³. To optimize ultrasound imaging and to prevent major leakage, the model was printed at a 70% infill. The STL models were sliced into horizontal layers via Slic3r, an open-source software, to produce a 3D-printing programming language (G-code), which determined the printing pathways. The G-code was entered into a customized 3D-printing system (AGS1000, Aerotech), fitted with two independent z-axis heads, which held two ink syringe barrels (Optimum, Nordson EFD) individually containing the supporting and polymeric ink. The rate of deposition was dictated by two high-accuracy dispensers (Ultimus V, Nordson EFD). Precision nozzles (Nordson EFD) with inner diameters of 0.84 mm (18 GA GP.013X.25) and 0.41 mm (22 GA GP.016X.25) were used to print layers with heights ranging from 0.7 to 0.3 mm, respectively. After the printed model has been fully cured at room temperature, the supporting ink was removed from the model via water flushing at 4°C.

4.4 | Fabrication of McKibben Actuators

A thermoplastic elastomer (TPE) bladder, polyurethane tubing, and a PET expandable braided mesh were used to fabricate

the actuators. The TPE bladder was obtained from Fibre Glast Developments Corporation. Polyurethane tubing was acquired from McMaster-Carr. A 0.25 inch PET mesh was purchased from TechFlex. Two equal sections of TPE were first heat-sealed, leaving a small opening for inserting the tubing. After the tubing was positioned, the seal was carefully formed around it to prevent leakage within the actuator. The bladder was then wrapped with PET mesh, and the ends of the assembled actuator were sealed. Finally, the actuators were tested at various pressures to identify any major leaks. These devices were prepared at different lengths according to the size of the gap present in the heart model. The actuators are embedded around the left ventricle (inside of the ventricle wall), being placed in designed inlets that wrap around the 3D-printed model. High-accuracy digital dispensers (Ultimus V, Nordson EFD) were used to apply pressure on the actuators, enabling them to axially contract and radially expand.

4.5 | Pressure Measurements

The customized pressure sensor with a piezoresistive layer and water resistance was designed to record pressures in the diastolic and systolic phases in the left ventricle of the heart model through the outlet, localized in the top section of the ventricle, where contraction is more prevalent. Here, the electrode (DuPont Pyralux AC 352500), composed of polyimide and copper, was overlaid with a piezoresistive material (Velostat), whose resistance changes under mechanical strain and can be interpreted as pressure. Then, polyimide tape was used to cover the region of the sensor that is exposed to blood-mimicking fluid, including the piezoresistive layer. This protective layer was added because the sensor is exposed to a blood-mimicking fluid that could otherwise cause a short circuit. Finally, to enable electrical interfacing, a section of the sensor layer remained uncovered, serving as the contact area for the voltmeter. Laser cutting was used to produce a highly precise sensor, reducing disruption to the heart model's flow and contraction dynamics when placed within the chambers for pressure recording. Following fabrication, the sensor underwent calibration by applying varying pressures using weights, and the resulting resistance changes were used to derive pressure values representative of cardiac conditions. This aided in reproducing pressure values in the heart model. Due to the dimensions of the model (5 × 5 mm²), 40 g of weight was applied to replicate 16 kPa of pressure (~120 mmHg) in the calibration process. Prior to pressure measurements, the ultrasound access cut-out was sealed to minimize pressure leakage (as a closed system), and a small incision was introduced in the atrium to serve as an inlet. Intraventricular pressure waveforms were subsequently recorded from the left ventricle.

4.6 | Imaging and Hemodynamic Measurements

Ultrasound imaging was provided by a Philips CX50 portable ultrasound. A Phillips S12-4 Transducer recorded the images from the atrium of the model, used to visualize the mitral valve during contraction. Endoscopic imaging was recorded using a Hijoy S20 Articulating Borescope. This endoscope device was run through the inlet of the heart model located on the atrium to visualize the mitral valve from above. A Golander BT 101S Variable-Speed Peristaltic Pump was used to input a flow of 511 mL/min into the

heart model. Stroke volume and ejection fraction were quantified using volumetric measurements of the left ventricle. The ventricle was first filled at maximum capacity, and the obtained volume was defined as the end-diastolic volume. During actuation, the volume of fluid expelled from the ventricle was collected and measured, corresponding to the stroke volume. The ejection fraction was then calculated as the ratio of stroke volume to end-diastolic volume.

Acknowledgements

Prof. K. Qiu acknowledges Startup Funds, Cougar Cage Funds, and Commercialization Special Project Funds from Washington State University and National Science Foundation (DGE #2244082). The authors thank Dr. Arda Gozen and Dr. Kimberlee Hughes in the Engineering Teaching Research Laboratory (ETRL) Building at WSU for assistance in mechanical testing.

Conflicts of Interest

The authors declare no conflicts of interest.

Data Availability Statement

The data that support the findings of this study are available from the corresponding author upon reasonable request.

References

1. A. Stefanovska and M. Bračić, "Physics of The Human Cardiovascular System," *Contemporary Physics* 40 (1999): 31–55.
2. M. Uehara and K. K. Sakane, "Physics Of The Cardiovascular System: An Intrinsic Control Mechanism Of The Human Heart," *American Journal of Physics* 71 (2003): 338–344.
3. S. S. Virani, A. Alonso, H. J. Aparicio, et al., "Heart Disease and Stroke Statistics—2021 Update," *Circulation* 143 (2021): E254.
4. F. B. Ahmad and R. N. Anderson, "The Leading Causes of Death in the US for 2020," *Jama* 325 (2021): 1829.
5. "Heart Disease Facts," Centers for Disease Control and Prevention can be found under <https://www.cdc.gov/heart-disease/data-research/facts-stats/index.html> (Accessed: October, 2024).
6. S. M. Dunlay, S. M. Manemann, A. M. Chamberlain, et al., "Activities of Daily Living and Outcomes in Heart Failure," *Circulation: Heart Failure* 8 (2015): 261–267.
7. K. M. Farooqi, C. G. Lengua, A. D. Weinberg, J. C. Nielsen, and J. Sanz, "Blood Pool Segmentation Results in Superior Virtual Cardiac Models Than Myocardial Segmentation for 3D Printing," *Pediatric Cardiology* 37 (2016): 1028–1036.
8. C. Vannelli, J. Moore, J. McLeod, D. Ceh, and T. Peters, "Dynamic Heart Phantom With Functional Mitral And Aortic Valves," in *Medical Imaging 2015: Image-Guided Procedures, Robotic Interventions, and Modeling* (SPIE, 2015).
9. M. S. Sacks, A. Drach, C. H. Lee, et al., "On the Simulation of Mitral Valve Function in Health, Disease, and Treatment," *Journal of Biomechanical Engineering* 141 (2019): 0708041.
10. G. Haghiashtiani, K. Qiu, J. D. Z. Sanchez, et al., "3D Printed Patient-Specific Aortic Root Models With Internal Sensors For Minimally Invasive Applications," *Science Advances* 6 (2020): 4641.
11. B. Zevin, R. Aggarwal, and T. P. Grantcharov, "Surgical Simulation in 2013: Why Is It Still Not the Standard in Surgical Training?," *Journal of the American College of Surgeons* 218 (2014): 294–301.

12. G. Biglino, C. Capelli, J. Wray, et al., "3D-Manufactured Patient-Specific Models Of Congenital Heart Defects For Communication In Clinical Practice: Feasibility And Acceptability," *BMJ Open* 5 (2015): 007165, <https://doi.org/10.1136/BMJOPEN-2014-007165>.
13. A. H. Sadeghi, S. el Mathari, D. Abjigitova, et al., "Current and Future Applications of Virtual, Augmented, and Mixed Reality in Cardiothoracic Surgery," *The Annals of Thoracic Surgery* 113 (2022): 681–691.
14. A. H. Sadeghi, S. el Mathari, D. Abjigitova, et al., "Current and Future Applications of Virtual, Augmented, and Mixed Reality in Cardiothoracic Surgery," *The Annals of Thoracic Surgery* 113 (2022): 681–691.
15. L. Perl, E. Soifer, J. Bartunek, et al., "A Novel Wireless Left Atrial Pressure Monitoring System for Patients With Heart Failure, First Ex-Vivo and Animal Experience," *Journal of Cardiovascular Translational Research* 12 (2019): 290–298.
16. E. Mirdamadi, J. W. Tashman, D. J. Shiwarski, R. N. Palchesko, and A. W. Feinberg, "Fresh 3D Bioprinting a Full-Size Model of the Human Heart," *ACS Biomaterials Science & Engineering* 6 (2020): 6453–6459.
17. P. P. Stankey, K. T. Kroll, A. J. Ainscough, et al., "Embedding Biomimetic Vascular Networks via Coaxial Sacrificial Writing Into Functional Tissue," *Advanced Materials* 36 (2024): 2401528.
18. B. Brady, G. King, R. T. Murphy, and D. Walsh, "Myocardial Strain: A Clinical Review," *Irish Journal of Medical Science (1971)* 192 (2023): 1649–1656.
19. M. E. Kupfer, W. H. Lin, V. Ravikumar, et al., "In Situ Expansion, Differentiation, and Electromechanical Coupling of Human Cardiac Muscle in a 3D Bioprinted, Chambered Organoid," *Circulation Research* 127 (2020): 207–224.
20. I. Badash, K. Burt, C. A. Solorzano, and J. N. Carey, "Innovations In Surgery Simulation: A Review Of Past, Current And Future Techniques," *Annals of Translational Medicine* 4 (2016): 23, [10.21037/ATM.2016.12.24](https://doi.org/10.21037/ATM.2016.12.24).
21. S. A. Cardoso, J. Suyambu, J. Iqbal, et al., "Exploring the Role of Simulation Training in Improving Surgical Skills Among Residents: A Narrative Review," *Cureus* 15 (2023): 44654, <https://doi.org/10.7759/CUREUS.44654>.
22. "FDA Announces Plan to Phase out Animal Testing Requirement for Monoclonal Antibodies and Other Drugs," Food and Drug Administration, April 10, 2025, can be found under <https://www.fda.gov/news-events/press-announcements/fda-announces-plan-phase-out-animal-testing-requirement-mono-clonal-antibodies-and-other-drugs>.
23. I. Gokhan, T. S. Blum, and S. G. Campbell, "Engineered Heart Tissue: Design Considerations and the State of the Art," *Biophysics Reviews* 5 (2024): 021308.
24. E. C. H. van Doorn, J. H. Amesz, O. C. Manintveld, et al., "Advancing 3D Engineered In Vitro Models for Heart Failure Research: Key Features and Considerations," *Bioengineering* 11 (2024): 1220.
25. J. M. Bliley, M. A. Stang, A. Behre, and A. W. Feinberg, "Advances in 3D Bioprinted Cardiac Tissue Using Stem Cell-Derived Cardiomyocytes," *Stem Cells Translational Medicine* 13 (2024): 425–435.
26. M. Chingale, K. Cheng, and K. Huang, "3D Bioprinting Technology—One Step Closer Towards Cardiac Tissue Regeneration," *Frontiers in Materials* 8 (2022): 804134.
27. S. J. Yoo, T. Spray, E. H. Austin, T. J. Yun, and G. S. van Arsdell, "Hands on Surgical Training of Congenital Heart Surgery Using 3-Dimensional Print Models," *The Journal of Thoracic and Cardiovascular Surgery* 153 (2017): 1530–1540.
28. C. Karsenty, A. Guitarte, Y. Dulac, et al., "The Usefulness of 3D Printed Heart Models for Medical Student Education in Congenital Heart Disease," *BMC Medical Education* 21 (2021): 480.
29. N. H. Cohrs, A. Petrou, M. Loepfe, et al., "A Soft Total Artificial Heart—First Concept Evaluation on a Hybrid Mock Circulation," *Artificial Organs* 41 (2017): 948–958.
30. J. Davies, M. T. Thai, B. Sharma, et al., "Soft Robotic Artificial Left Ventricle Simulator Capable of Reproducing Myocardial Biomechanics,"

- Science Robotics* 9 (2024): ado4553, <https://doi.org/10.1126/SCIROBOTICS.ADO4553>.
31. E. T. Roche, M. A. Horvath, I. Wamala, et al., "Soft Robotic Sleeve Supports Heart Function," *Science Translational Medicine* 9 (2017): aaf3925, <https://doi.org/10.1126/SCITRANSLMED.AAF3925>.
 32. M. Singh, J. Bonnemain, C. Ozturk, et al., "Robotic Right Ventricle is a Biohybrid Platform That Simulates Right Ventricular Function in (patho)Physiological Conditions and Intervention," *Nature Cardiovascular Research* 2 (2023): 1310–1326.
 33. S. B. Brown, A. Raina, D. Katz, M. Szerlip, S. E. Wieggers, and P. R. Forfia, "Longitudinal Shortening Accounts for the Majority of Right Ventricular Contraction and Improves After Pulmonary Vasodilator Therapy in Normal Subjects and Patients With Pulmonary Arterial Hypertension," *Chest* 140 (2011): 27–33.
 34. L. Rosalia, C. Ozturk, D. Goswami, et al., "Soft Robotic Patient-Specific Hydrodynamic Model of Aortic Stenosis And Ventricular Remodeling," *Science Robotics* 8 (2023): ade2184, <https://doi.org/10.1126/SCIROBOTICS.ADE2184>.
 35. P. T. Phan, M. T. Thai, T. T. Hoang, N. H. Lovell, and T. N. Do, "HFAM: Soft Hydraulic Filament Artificial Muscles for Flexible Robotic Applications," *IEEE Access* 8 (2020): 226637–226652.
 36. H. Shi, K. Tan, B. Zhang, and W. Liu, "Review on Research Progress of Hydraulic Powered Soft Actuators," *Energies* 15 (2022): 9048.
 37. S. Okhovatian, M. H. Mohammadi, N. Rafatian, and M. Radisic, "Engineering Models of the Heart Left Ventricle," *ACS Biomaterials Science & Engineering* 8 (2022): 2144–2160.
 38. S. Maglio, C. Park, S. Tognarelli, A. Menciassi, and E. T. Roche, "High-Fidelity Physical Organ Simulators: From Artificial to Bio-Hybrid Solutions," *IEEE Transactions on Medical Robotics and Bionics* 3 (2021): 349–361.
 39. A. M. Leopaldi, K. Wrobel, G. Speziali, S. van Tuijl, A. Drasutiene, and W. R. Chitwood, "The Dynamic Cardiac Biosimulator: A Method For Training Physicians In Beating-Heart Mitral Valve Repair Procedures," *The Journal of Thoracic and Cardiovascular Surgery* 155 (2018): 147–155.
 40. M. Davey, C. Puelz, S. Rossi, et al., "Simulating Cardiac Fluid Dynamics in the Human Heart," *PNAS Nexus* 3 (2024): pgae392, <https://doi.org/10.1093/PNASNEXUS/PGAE392>.
 41. H. Wang, H. Song, Y. Yang, et al., "Three-Dimensional Printing for Cardiovascular Diseases: From Anatomical Modeling to Dynamic Functionality," *Biomedical Engineering Online* 19 (2020): 76.
 42. N. S. Birbara, J. M. Otton, and N. Pather, "3D Modelling and Printing Technology to Produce Patient-Specific 3D Models," *Heart, Lung and Circulation* 28 (2019): 302–313.
 43. K. Capellini, L. Ait-Ali, V. Pak, et al., "Three-Dimensional Printed Models As An Effective Tool for the Management of Complex Congenital Heart Disease," *Frontiers in Bioengineering and Biotechnology* 12 (2024): 1369514.
 44. K. S. A. Yakof, N. F. Zabudin, I. Mat Sahat, and M. A. H. Mohd Adib, "Development of 3D Printed Heart Model for Medical Training," in *Lecture Notes in Mechanical Engineering* (Springer, 2018), 109–116.
 45. K. Qiu, Z. Zhao, G. Haghiashiani, et al., "3D Printed Organ Models With Physical Properties of Tissue and Integrated Sensors," *Advanced Materials Technologies* 3 (2018): 1700235.
 46. E. S. Chen, A. Ahmadianshalchi, S. S. Sparks, et al., "Machine Learning Enabled Design and Optimization for 3D-Printing of High-Fidelity Presurgical Organ Models," *Advanced Materials Technologies* 10 (2025): 2400037.
 47. Z. Lyu, J. J. Koh, G. J. H. Lim, et al., "Direct Ink Writing of Programmable Functional Silicone-Based Composites for 4D Printing Applications," *Interdisciplinary Materials* 1 (2022): 507–516.
 48. "How the Heart Works—How Blood Flows Through the Heart," National Heart, Lung, and Blood Institute, can be found under <https://www.nhlbi.nih.gov/health/heart/blood-flow>.
 49. A. Constantine and K. Dimopoulos, "Physiology of the Normal Heart," *Medicine* 50 (2022): 322–326.
 50. P. W. Armstrong, "Left Ventricular Dysfunction: Causes, Natural History, And Hopes For Reversal," *Heart* 84 (2000): i15–i17.
 51. R. A. Levine, A. A. Hagège, D. P. Judge, et al., "Mitral Valve Disease—Morphology And Mechanisms," *Nature Reviews Cardiology* 12 (2015): 689–710.
 52. F. Martini, A. Zuppiroli, A. M. Gori, et al., "Platelet And Blood Clotting Activation In Patients With Mitral Valve Prolapse," *Thrombosis Research* 83 (1996): 299–306.
 53. W. H. Gaasch and T. E. Meyer, "Left Ventricular Response to Mitral Regurgitation," *Circulation* 118 (2008): 2298–2303.
 54. A. El Sabbagh, Y. N. V. Reddy, and R. A. Nishimura, "Mitral Valve Regurgitation in the Contemporary Era," *JACC: Cardiovascular Imaging* 11 (2018): 628–643.
 55. A. H. Khalighi, A. Drach, C. H. Bloodworth, et al., "Mitral Valve Chordae Tendineae: Topological and Geometrical Characterization," *Annals of Biomedical Engineering* 45 (2017): 378–393.
 56. D. Zrinscak, C. M. De Chirico, L. Lorenzon, et al., "Design of a Soft Robotic Artificial Cardiac Wall," *Artificial Organs* 49 (2025): 1265–1276.
 57. J. Davies, M. T. Thai, B. Sharma, et al., "Soft Robotic Artificial Left Ventricle Simulator Capable Of Reproducing Myocardial Biomechanics," *Science Robotics* 9 (2024): ado4553, <https://doi.org/10.1126/SCIROBOTICS.ADO4553>.
 58. A. Ilina, A. Lasso, and M. A. Jolley, "Patient-Specific Pediatric Silicone Heart Valve Models Based on 3D Ultrasound," in *Medical Imaging 2017: Image-Guided Procedures, Robotic Interventions, and Modeling* (SPIE, 2017), 10135, <https://doi.org/10.1117/12.2255849>.
 59. B. Peel, W. Lee, N. Hussein, and S. J. Yoo, "State-of-the-Art Silicone Molded Models for Simulation of Arterial Switch Operation: Innovation With Parting-And-Assembly Strategy," *JTCVS Techniques* 12 (2022): 132–142.
 60. N. H. Cohrs, A. Petrou, M. Loeffe, et al., "A Soft Total Artificial Heart—First Concept Evaluation on a Hybrid Mock Circulation," *Artificial Organs* 41 (2017): 948–958.
 61. M. Davey, C. Puelz, S. Rossi, et al., "Simulating Cardiac Fluid Dynamics In The Human Heart," *PNAS Nexus* 3 (2024), <https://doi.org/10.1093/PNASNEXUS/PGAE392>.
 62. R. Kozdrach, J. Drabik, and M. Szczerek, "Influence of Silicon Additives on Tribological and Rheological Test Results for Vegetable Lubricants," *Materials* 16 (2023): 6245.
 63. H. Liu, P. Fan, F. Jin, G. Huang, X. Guo, and F. Xu, "Dynamic and Static Biomechanical Traits Of Cardiac Fibrosis," *Frontiers in Bioengineering and Biotechnology* 10 (2022): 1042030.
 64. B. Wu, P. Pu, S. Zhao, et al., "Frequency-Related Viscoelastic Properties of the Human Incisor Periodontal Ligament Under Dynamic Compressive Loading," *PLoS ONE* 15 (2020): 0235822.
 65. M. Siami, K. Jahani, and M. Rezaee, "Identifying The Parameters Of Viscoelastic Model for A Gel-Type Material as Representative of Cardiac Muscle in Dynamic Tests," *Proceedings of the Institution of Mechanical Engineers, Part H: Journal of Engineering in Medicine* 235 (2021): 1205–1216.
 66. K. Qiu, Z. Zhao, G. Haghiashiani, et al., "3D Printed Organ Models With Physical Properties of Tissue and Integrated Sensors," *Advanced Materials Technologies* 3 (2018): 1700235.
 67. "Frequency of a Beating Heart—The Physics Factbook," can be found under <https://hypertextbook.com/facts/1998/ArsheAhmed.shtml>.
 68. A. B. Goldstone and Y. J. Woo, "Alternative Approaches For Mitral Valve Repair," *Annals of Cardiothoracic Surgery* 4 (2015): 46973.
 69. A. A. Young and B. R. Cowan, "Evaluation of Left Ventricular Torsion by Cardiovascular Magnetic Resonance," *Journal of Cardiovascular Magnetic Resonance* 14 (2012): 56.

70. S. C. Obiajulu, E. T. Roche, F. A. Pigula, and C. J. Walsh, "Soft Pneumatic Artificial Muscles With Low Threshold Pressures for a Cardiac Compression Device," in *International Design Engineering Technical Conferences and Computers and Information in Engineering Conference* (The American Society of Mechanical Engineers, 2013), <https://doi.org/10.1115/DETC2013-13004>.
71. L. Bennati, V. Giamb Bruno, F. Renzi, et al., "Turbulent Blood Dynamics in the Left Heart in the Presence of Mitral Regurgitation: A Computational Study Based on Multi-Series Cine-MRI," *Biomechanics and Modeling in Mechanobiology* 22 (2023): 1829–1846.
72. A. Jagannathan, J. Micallef, T. Clarke, K. Armstrong, and A. Dubrowski, "The Iterative Design and Development of an Affordable Ultrasound Simulator," *Cureus* 16 (2024): 52300.
73. K. Potter, C. J. Reed, D. J. Green, G. J. Hankey, and L. F. Arnolda, "Ultrasound Settings Significantly Alter Arterial Lumen and Wall Thickness Measurements," *Cardiovascular Ultrasound* 6 (2008): 6.
74. D. G. Paeng, C. A. Lee, and C. Imtiaz, "Principles Of Doppler Ultrasound and Emerging Blood Flow Imaging," *Ultrasonography* 44 (2025): 409.
75. G. W. Stone, W. T. Abraham, J. Lindenfeld, et al., "Five-Year Follow-up After Transcatheter Repair of Secondary Mitral Regurgitation," *New England Journal of Medicine* 388 (2023): 2037–2048.
76. T. Feldman, S. Kar, M. Rinaldi, et al., "Percutaneous Mitral Repair With the MitraClip System," *Journal of the American College of Cardiology* 54 (2009): 686–694.
77. C. Park, M. Singh, M. Y. Saeed, C. T. Nguyen, and E. T. Roche, "Biorobotic Hybrid Heart As A Benchtop Cardiac Mitral Valve Simulator," *Device* 2 (2024): 100217, <https://doi.org/10.1016/j.device.2023.100217>.
78. W. J. Corin, T. Murakami, E. S. Monrad, O. M. Hess, and H. P. Krayenbuehl, "Left Ventricular Passive Diastolic Properties In Chronic Mitral Regurgitation," *Circulation* 83 (1991): 797.
79. Y. Zhang, W. feng Yan, L. Jiang, et al., "Aggravation Of Functional Mitral Regurgitation on Left Ventricle Stiffness in Type 2 Diabetes Mellitus Patients Evaluated by CMR Tissue Tracking," *Cardiovascular Diabetology* 20 (2021): 1.
80. K. Aycock, K. Blinova, and M. Casciola, "Cardiovascular Medical Devices: Regulatory Science Research Overview in the Office of Science and Engineering Laboratories (OSEL) at the Food and Drug Administration (FDA)," in *Proceedings of the 2021 Design of Medical Devices Conference* (American Society of Mechanical Engineers, 2021), <https://doi.org/10.1115/DMD2021-1085>.

Supporting Information

Additional supporting information can be found online in the Supporting Information section.

Supporting File 1: admt70885-sup-0001-SuppMat.docx.

Supporting File 2: admt70885-sup-0002-MovieS1.mp4.

Supporting File 3: admt70885-sup-0003-MovieS2.mp4.

Supporting File 4: admt70885-sup-0004-MovieS3.mp4.

Supporting File 5: admt70885-sup-0005-MovieS4.mp4.

Supporting File 6: admt70885-sup-0006-MovieS5.mp4.